Supplementary Information for: Structural colouring and luminescence anisotropy of perovskite thin films via laser-induced periodic surface structure formation

Aleksandra Furasova*,[†,‡] Yaroslava Andreeva,[‡,#] Jiangnan Xing,[‡,†] Xiaohan Chen,[†] Valeriy Kondratev,[¶,§] Qinghao Song,[‡] Ivan Vazhenin,[‡] Evgeniia Stepanidenko,[‖] Vyacheslav Goncharov,[⊥] Sergei Cherevkov,[‖] Dmitry Permyakov,[‡] Dmitry Zhirihin,[‡] and Sergey V. Makarov*[,‡,†]

†*Qingdao Innovation and Development Center, Harbin Engineering University, Qingdao 266000, Shandong, China*

‡*School of Physics and Engineering, ITMO University, 197101, St. Petersburg, Russia*

¶*Moscow Center for Advanced Studies, Kulakova str. 20, Moscow 123592, Russia*

§*Center for Nanotechnologies, Alferov University, Khlopina 8/3, 194021 Saint Petersburg, Russia*

‖*PhysNano Department, ITMO University, 197101 Saint Petersburg, Russia*

⊥*Infochemistry Scientific Center, ITMO University, 9 Lomonosova Street, Saint-Petersburg 191002, Russia*

#*Institute of Laser Technologies, ITMO University, Saint Petersburg 197101*

E-mail: aleksandra.furasova@metalab.ifmo.ru,s.makarov@metalab.ifmo.ru

S1 Materials selection for LIPSS generation under 355 nm nanosecond laser

In order to determine the optimal material for gomogenious LiPSS gratings preparation for potential applications in photovoltaic thin-film solar devices, a series of experiments was conducted. The same laser system was used, and exposure parameters such as pulse repetition rate, scanning speed, and radiation power were varied over a wide range.

We applied periodic structures to different layers which is usually used to fabricate perovskite PV devices (LEDs, solar cells, photodetectors and etc.) and compared the morphology of the resulting gratings, as well as the laser formation parameters. The article details the best results obtained from recording lattices on TiO_2 films. However, it should be noted that preliminary experiments on LIPSS formation on FTO, ITO, and directly on perovskite films were conducted first. The first step for all these attempts was to find parametric gaps for material modification. For this, we applied arrays of small squares with the density of scan lines along Y axis of 100 lin/mm, scan speed of 50 mm/s and two different pulse repetition rates of 150 and 300 kHz. We changed laser mean power from 0.01 to 2.58 W to find modification thresholds.

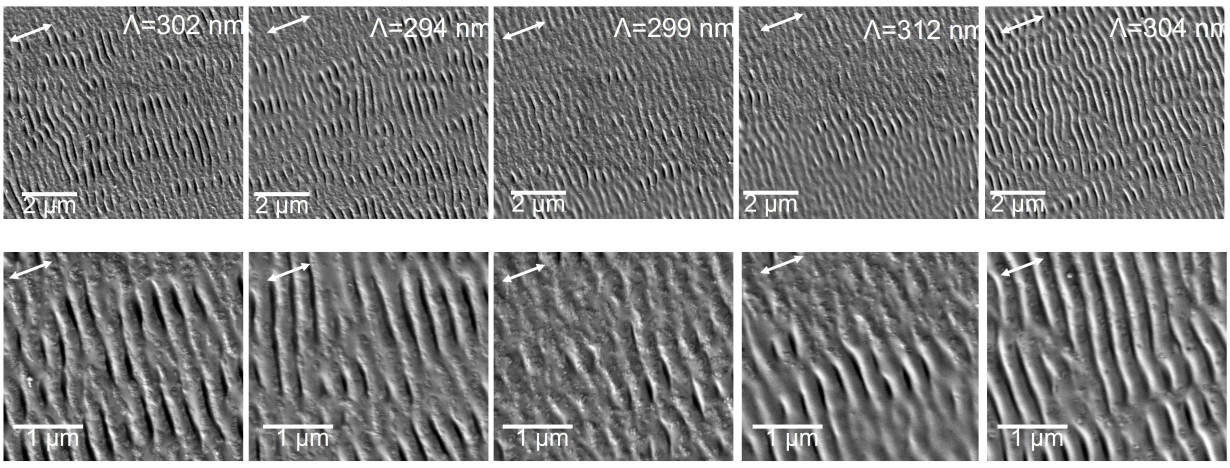

Figure S1: Scanning electron microscopy images of periodic structured uncovered FTO films on glass using UV ns laser (F=238.4 mJ/cm^2, V_{sc} = 300 – 500 mm/s)

We have shown that the application of periodic lattices is also possible for the FTO layer. In this case we used scan speed range from 300 to 500 mm/s, and laser fluences of F 230-300 mJ/cm^2 were needed for recording. The periodic structures obtained using pure FTO for laser fluence F=238.4 mJ/cm^2 and different scan speed are shown in Fig. S3S1. It was possible to create lattices with a period ranging from 295 to 315 nm in this case. The energy thresholds for forming these structures were significantly higher, and the structures themselves appeared less uniform and more damaged. This is due to the different excitation conditions of surface plasmon-polaritons at the air-TiO_2 and air-FTO interfaces, resulting from the difference in dielectric constants of these materials, as well as the different absorption coefficients of the films.

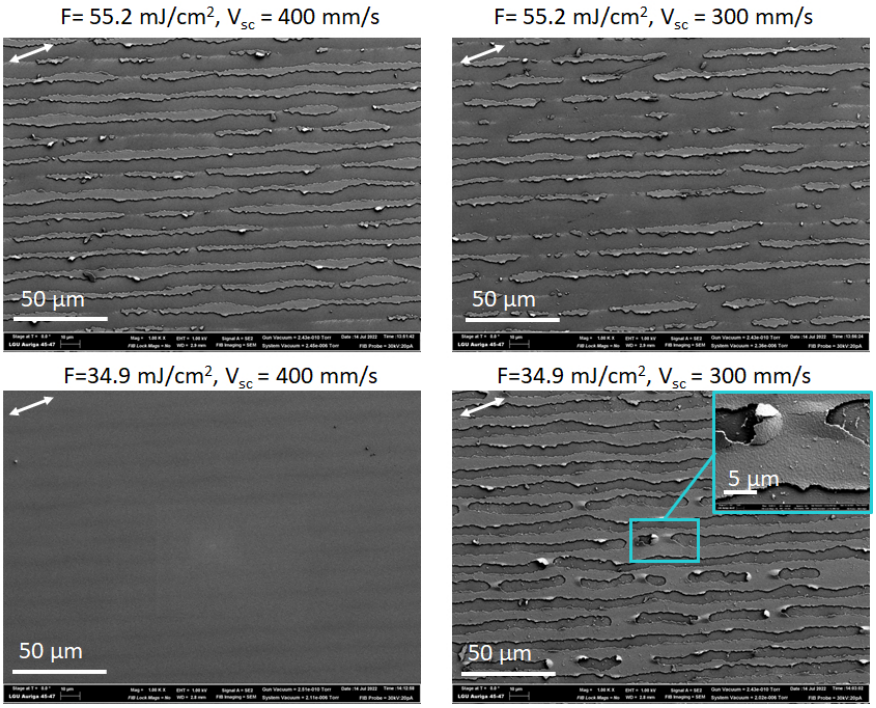

Figure S2: Scanning electron microscopy images of Periodic structures obtained on ITO+SnO_2 film on glass using UV ns laser (F = 34.9 mJ/cm^2, 55.2 mJ/cm^2, V_{sc} = 300, 400 mm/s)

Several attempts have also been made to fabricate periodic structures on ITO glass, but in this case, the resulting gratings were ever caused by the destruction of ITO and separation of the films under the laser radiation or have not even appeared. Even additional layer of

SnO_2 does not prevent melting of ITO contact. Note, that spray deposition of TiO_2 is not suitable for ITO due to a material instability at 460 C temperature. Figure S2 demonstrates such destructive periodical gratings recorded on ITO+SnO_2 film with relatively low fluences (F=34.9 mJ/cm^2, 55.2 mJ/cm^2, V_{sc} = 300, 400 mm/s). A film cracking might be caused by low adhesion of ITO on glass substrate.

Nevertheless, at scanning condition with F=34.9 mJ/cm^2 and V_{sc} = 400 mm/s LIPSS structures appear on ITO+SnO_2 films.

S2 Photographs of FTO-TiO_2-perovskite nanostructuring films

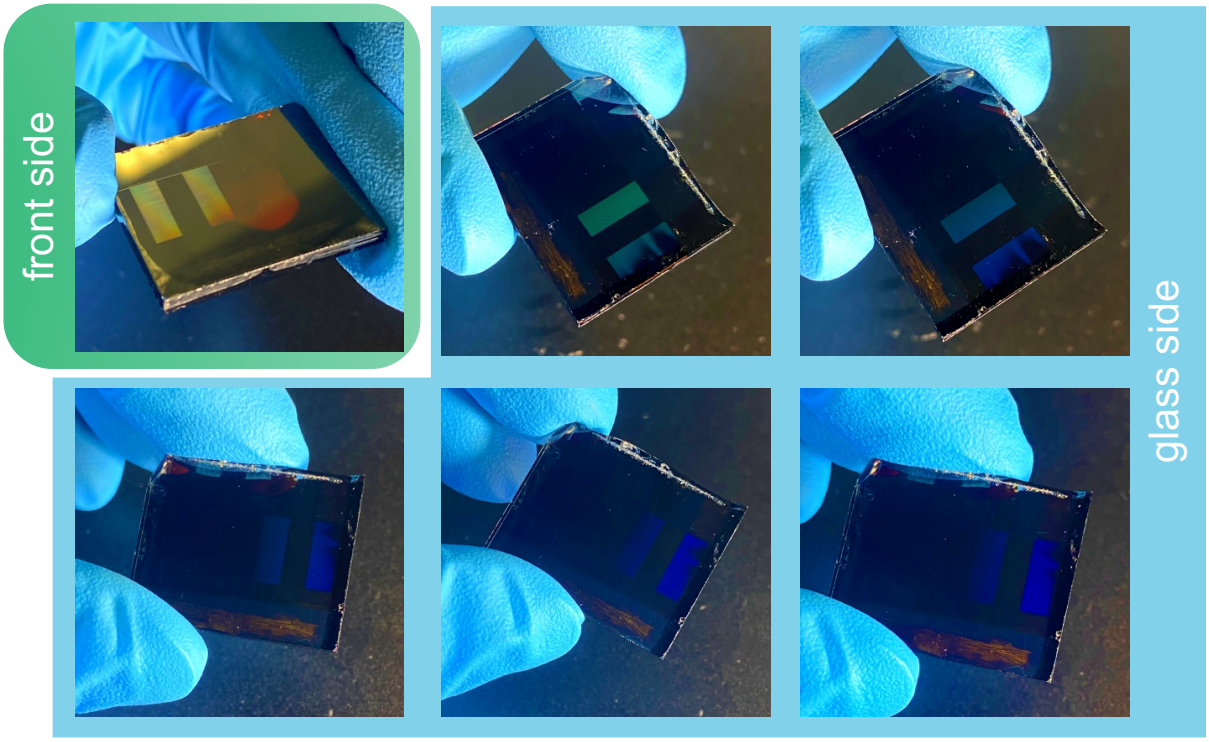

Figure S3: View of 3-ple cation perovskite film deposited on FTO-TiO_2 glass with and without LIPSS areas. Images are from the perovskite side and from the glass side illuminated by 4000 K white light under different angles.

Photographs presents CsMAFAPb$(IBr)_3$ film on FTO-TiO_2 with two LIPSS cells recorded under UV (355 nm) nanosecond laser-assisted process with period of 290±10 nm at laser scanning parameters: F=184 mJ/cm^2, V_{SC} = 350 mm/s. Images in Figure S3 demonstrate the scattering of light from the perovskite with and without LIPSS, illuminated by a 4000 K white light source, at different light rotation.

In general 3-ple cation perovskite film compositions have dark brown color due to their light absorption properties. When these films cover of a LIPSS area they scatter the selected light range.

S3 Experimental setup scheme of PL measurements under different angles

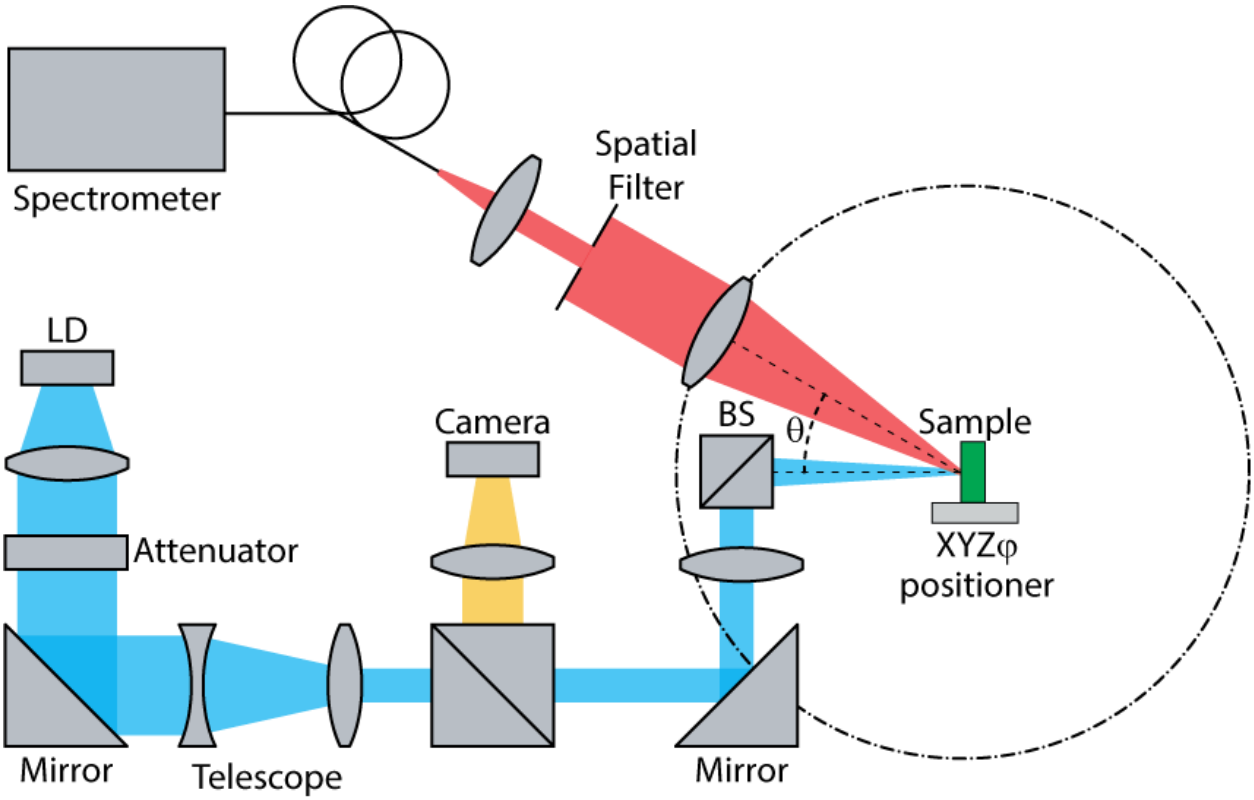

Figure S4: Experimental setup scheme for polarized PL light detection. LD – laser diode. BS – beam splitter. Θ is the angle of rotation of the collection channel

A continious wave laser-diode with a wavelength of 405 nm was used as the radiation source. The radiation power was then controlled using a variable ND filter; the power was 5 mW. The radiation was down-sized with the telescope and focused on the sample using a lens with f = 150 mm. The sample was mounted on a three-coordinate translator with the possibility of additional rotation in the plane perpendicular to excitation optical axis. A luminescent signal was collected with a lens with f = 150 mm, filtrated with the pinhole with d = 1mm and analyzed with a fiber spectrometer (AvaSpec-2048 Avantes). The collection channel was rotated all around the sample. The sample was oriented in two positions: the grating was oriented perpendicular (1) and parallel (2) to the scanning plane. The total incoming error at 360 rotation is no more than 0.5. Due to all these factors, it was decided to measure the photoluminescence spectra in 1 increments. A similar experimental setup was presented by Solomonov A. I. et al[1]

S4 Calculated far field of perovskite film when dipole is on a different height inside perovskite

Here the far field diagrams have been prepared as an average of 3 directions of a dipole placed close to TiO_2 (bottom graphs) and in the middle of a perovskite film (upper diagrams). The current place of the dipole highly affects on field propagation. When the dipole is placed close to TiO_2 LIPSS, the back output is suppressed and direct output becomes narrower. In this case, the number of highs and lows increases for the $CsPbBr_3$ based QD's film. The nanostructured $CsMAFAPbIBr_3$ film has a field distribution without clearly expressed maximums and minimums but its field propagation has a similar manner to become more narrow when the dipole is close to LIPSS.

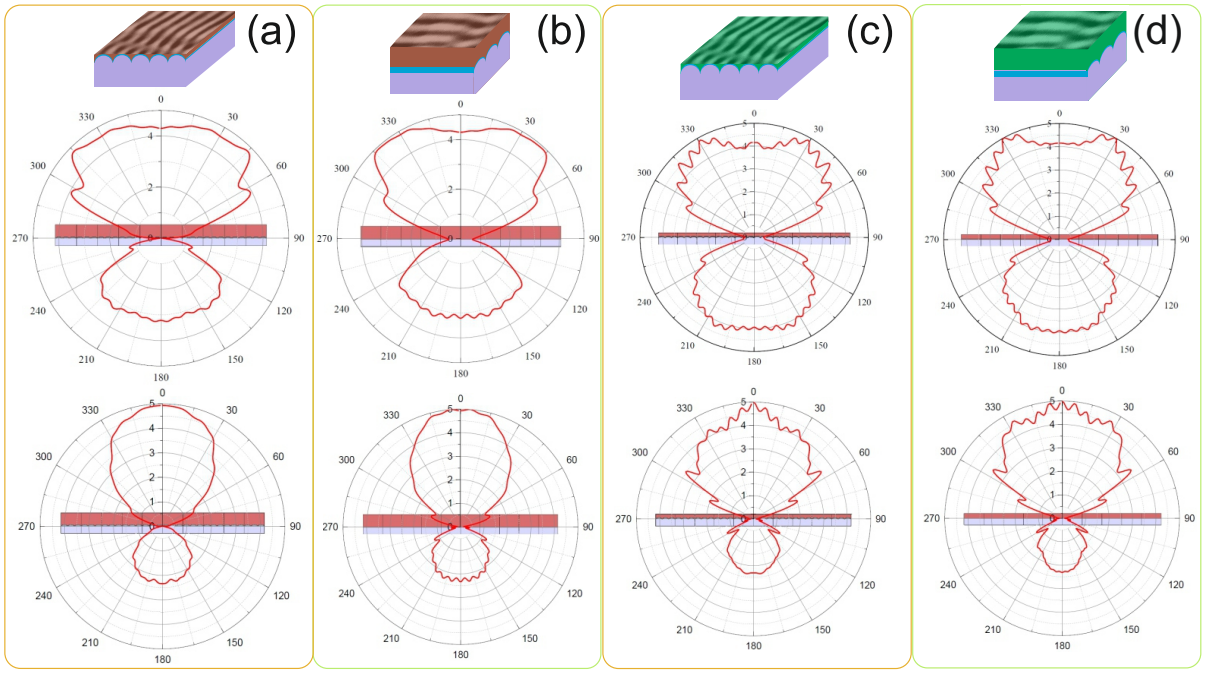

Figure S5: Calculated far field perovskite nanostructured films: LIPSS - $CsFAMAPb(IBr)_3$ film when a dipole at front (a) and sagittal (b) plane of LIPSS when it is placed close to TiO_2 or in the middle of perovskite. Far field for $CsPbBr_3$ quantum dot films placed on the LIPSS layer at front (c) and sagittal (d) plane of LIPSS when it is placed close to TiO_2 or in the middle of the $CsPbBr_3$ layer

S5 Reprodusibility of laser writing conditions on different FTO-TiO_2 films

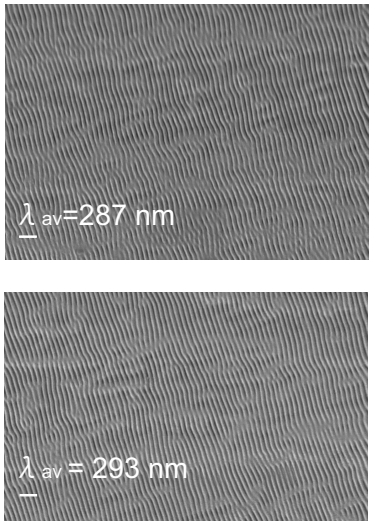

Figure S6: Wide-view scanning electron microscopy images from different samples at optimized laser writing parameters of TiO_2 LIPSS. Scale bar 1 μm

Figure S6 presents SEM of homogeneous LIPSS array scanned from different samples.

S6 Reflection on TiO_2 LIPSS

Angle-resolved reflectance measurements show that the reflection spectra of LIPSS at 9 degree decreases but this value becomes higher with the angle of the sample rotation.

The changes in the reflection spectrum is a result of light diffraction on LIPSS.

S7 X-ray powder diffraction of $CsFAMAPb(IBr)_3$ on planar TiO_2 layer and TiO_2 LIPSS

X-ray diffraction (XRD) analysis was performed using a D2 PHASER diffractometer (Bruker, Germany) with CuKα radiation ($\lambda = 1.54184$ Å), operating at a tube voltage of 30 kV and

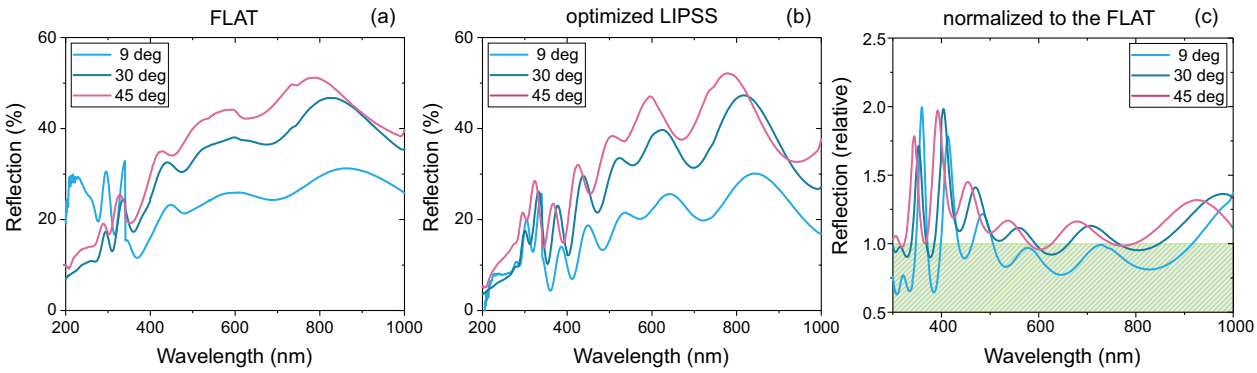

Figure S7: Reflection spectra for FTO-TiO_2 flat (a) and LIPSS (b) films and their comparison(c) reordered at 9, 30, 45 degree of the sample rotation

a current of 10 mA, in Bragg–Brentano geometry, equipped with a LYNXEYE (SSD160-2) detector. The 2θ range was set from 8° to 40°, with a scanning speed of 2°/min and a step size of 0.02°. The sample was analyzed as a coating on a glass substrate at an ambient temperature. Data processing was performed using DIFFRAC.EVA software with background subtraction and peak fitting.

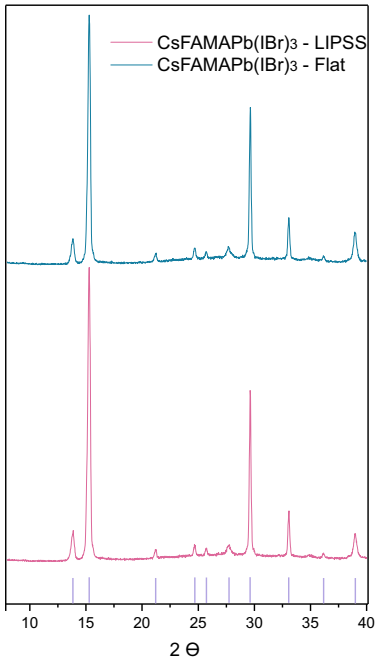

Figure S8: X-ray powder diffraction of $CsFAMAPb(IBr)_3$ perovskite films deposited on FTO-TiO_2 film with and without LIPSS area

$CsFAMAPb(IBr)_3$ perovskite polycrystal films form on TiO_2 surfaces. To check any influence of LIPSS on this perovskite crystallization, these samples (with and without LIPSS area) have been studied by X-ray powder diffraction method. Figure S8 shows that the $CsFAMAPb(IBr)_3$ X-ray spectra for two areas are similar, just some peaks for perovskite on LIPSS have a bit higher intensity: at 16, 29 degree.

S8 LIPSS formation and optimization on TiO_2 films

Modification of TiO_2 films for scan speed of 50 mm/s and f=150 kHz occurred at fluences ranging from 50 mJ/cm^2 to 700 mJ/cm^2, thus this interval was used for further experiments. We applied test arrays of small squares (200×200 μm) with different processing parameters: laser fluence of 56 to 622 mJ/cm^2, scan speed from 50 to 500 mm/s, the density of scan lines along the Y axis N_y of 50, 100 and 200 lin/mm and repetition rate f = 150 and 300 kHz).

Grating formation was checked by visual analysis first (the appearance of structural rainbow-like colors), and, if there are some diffraction effects, the samples were also observed by optical microscopy The parametric gaps for LIPSS formation were identified by optical microscopy in cross-polarized light. Figure S9 (a) shows the microphotograph of one of the arrays. The more pronounced optical anisotropy observed in cross-polarization mode the more uniform structure was. Thus, using microscopy it was possible to build the parametric map for the first experiment that is demonstrated in Fig. S9 (b). The green colored squares on the map indicate uniform LIPSS formation, while the yellow color means nonuniform structuring.

Our next goal was to find the parametric gaps for most uniform LIPSS formation on TiO_2. Several parametric gaps from the first stage were chosen with the most pronounced anisotropy of optical properties, and within these ranges the new arrays of test squares were recorded with the smaller step of changes. We have recorded several arrays of 300×300 μm squares with different scan speed 50-500 mm/s, pulse repetition rate of 150, 200 and 300 kHz,

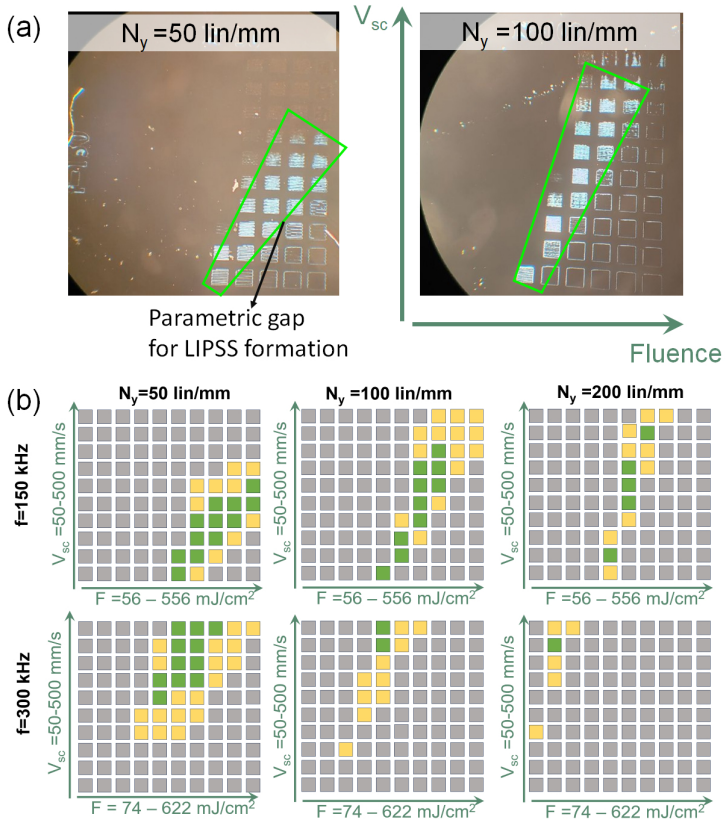

Figure S9: Results on TiO_2 laser modification: microphotograph of the recorded arrays for f=150 kHz, N_y=50, 100 lin/mm in the cross-polorized light. The green outline shows the region of LIPSS formation (a); parametric map for LIPSS formation: the green colored squares indicate uniform LIPSS and yellow nonuniform LIPSS, gray squares ae modification without LIPSS formation (for f=150, 300 kHz, V_{sc} = 50-500 mm/s, N_y 50, 100 and 200 lin/mm, and laser fluence of: 56 to 622 mJ/cm^2) (b)

the scan line density N_y of 100 and 200 lines per mm and fluence F = 72 – 370 mJ/cm^2. The parametric maps of the recorded arrays are shown in Figure S10.

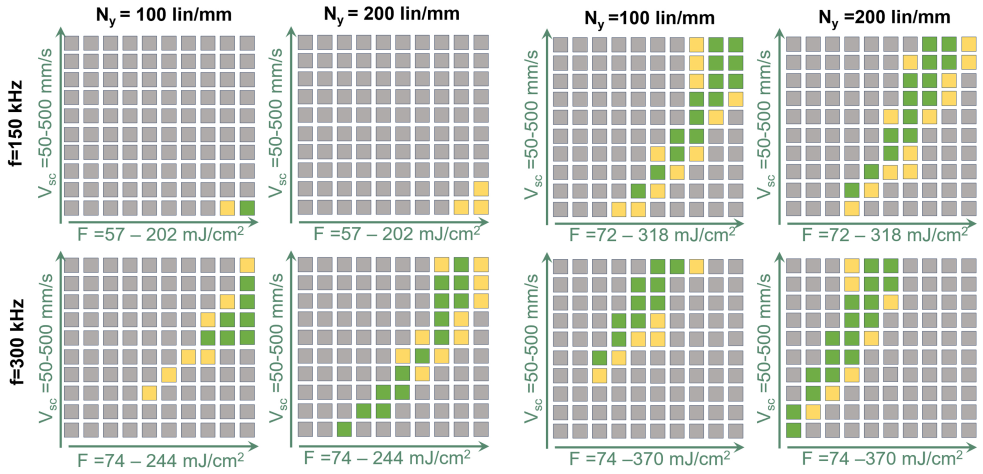

Figure S10: Parametric maps for LIPSS formation for f=150, 200 and 300 kHz, V_{sc} = 50 - 500 mm/s, N_y 100 and 200 lin/mm and laser fluence of F = 72 – 370 mJ/cm^2

The samples were also observed by optical microscopy (in cross-polarized mode), and the typical picture of such structures are shown in Fig. S11). The optical anisotropy, that can be detected as bright structures in cross-polarized mode, the brightness of which depends on rotation of structure (see Fig. S11 c), means the appearance of LIPSS. The more pronounced anisotropy indicates uniform continuous LIPSS.

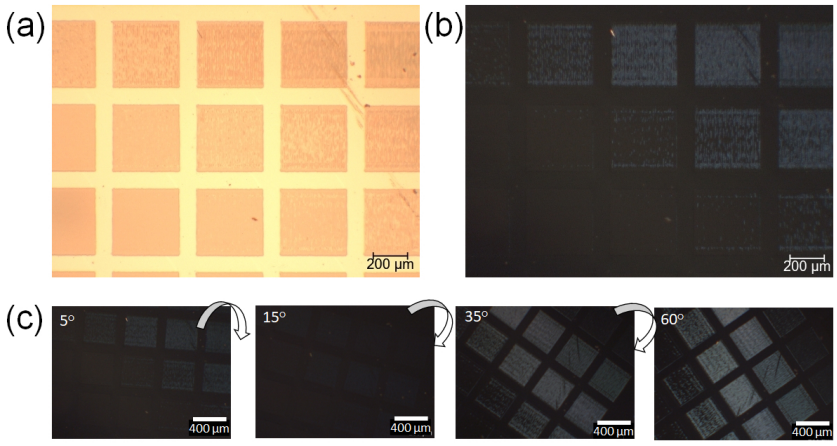

Figure S11: Microphotograph of a typical array of squares: in white light (a); in the cross-polarized light (b), in the cross-polarized light with rotation for different angles (c)

The third stage of our experiments was devoted to further optimization of parameters

to enhance uniformity of nanostructures, and speed performance. For this, we selected the fastest regimes from the previous arrays and recorded squares of 1×1 and 3×3 mm. Using SEM and optical microscopy, the most uniform structures were chosen and recorded for further SEM, AFM, and spectral investigations. These top 3 nanostructures with periods of 300±13 nm period (laser processing parameters F=324 mJ/cm^2, V_{sc} = 500 mm/s), 295±15 nm (F=360 mJ/cm^2, V_{sc} = 500 mm/s) and (c) 290±10 nm (F=184 mJ/cm^2, V_{sc} = 350 mm/s) are shown in Figure 2 in the Results and discussion section. The photographs of all the obtained test arrays with different structures on TiO_2 film are shown in Figure S12.

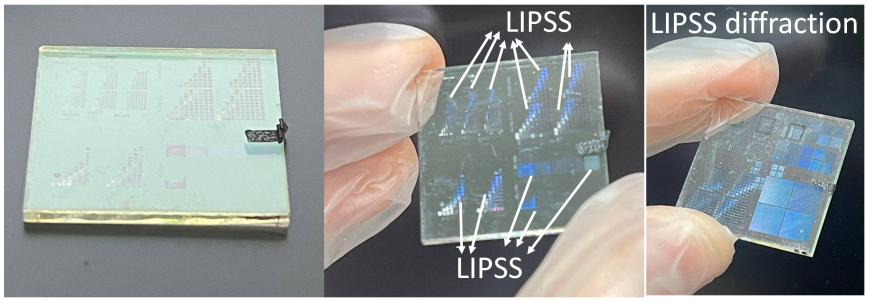

Figure S12: The photographs of obtained arrays of different structures on TiO_2 film. LIPSS formation is detected where diffraction of white light appears

S9 Angle - resolved TRPL measurements of perovskite films at different LIPSS orientation

We have conducted additional measurements of TRPL of perovskite films under different angles. The decay trend, as well as TRPL constants remain similar to the TRPL measurements with light detection at right angles (Figure 7), just PL signal has different intensity at the detector rotation and LIPSS orientation.

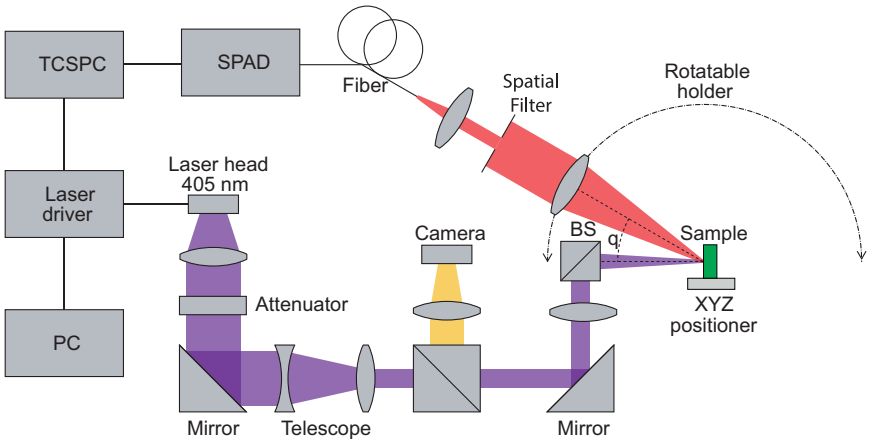

Figure S13: Experimental setup scheme for polarized TRPL signal detection. LD – laser diode. BS – beam splitter. q is the angle of rotation of the collection channel

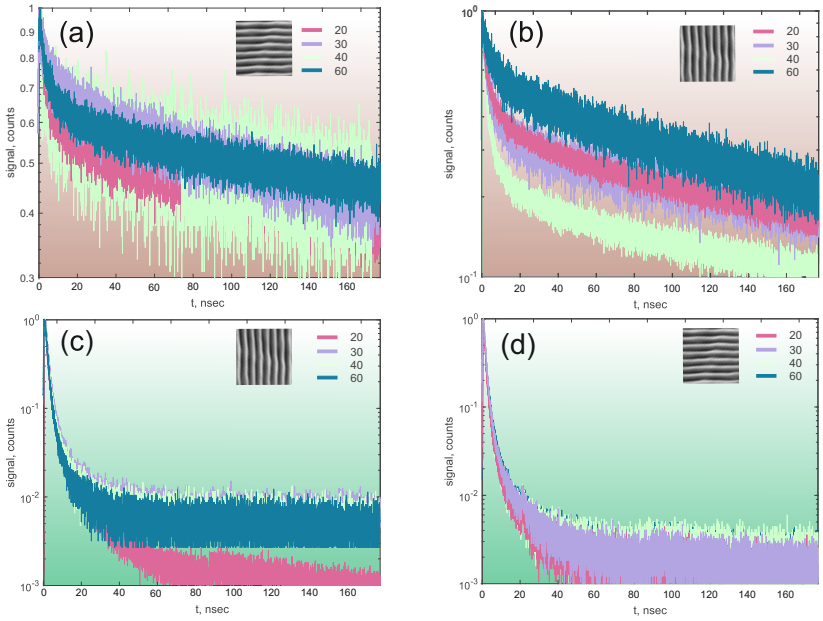

Figure S14: Time resolved photoluminescence dependence (a-d) on angle of rotation of the collection channel obtained from perovskite nanostructured films: (a) and (b) - $CsMAFAPbIBr_3$ $CsPbBr_3$ quantum dot films, (c) and (d) - $CsPbBr_3$ quantum dot films. The nanostructured perovskite films have been oriented in two positions: in parallel to the detector rotation (a, d) and perpendicular (b, c) to the scanning plane

S10 Experimental errors and their accounting

Perovskite synthesis: all perovskite solutions preparation error should be less than 5% (precursor weighting, solution mixing) to avoid bad or uniform crystallization of perovskite films. The reagents purity utilized in the current research presents in the experimental section. For antisolvent dropping the optimal time dispension is 15 s (± 1 s) before the end of spinning time to form current CsFAMAPb$(IBr)_3$ films. The perovskite film preparation part is more sensitive from a human factor. Taking this into account we have created LIPSS and LIPSS-free zones in one substrate to compare all PL and optical properties of selected perovskites. TiO_2 film preparation: the initial thickness of TiO_2 for LIPSS formation has 2 nm roughness; LIPSS formation: commercially available laser system was used for LIPSS formation that helped to avoid additional errors and instabilities. The laser scannator positioning error is ± 2 μm that is negligible for 2x3 cm area of the reported structures. The long-term avarage power instability is < 1.5 %, short-term pulse energy instability, RMS $< 2\%$. It is worth noting that all the experiments were repeated several times in order to obtain sufficient statistical data, and the repeatability was high, even for structures recorded on different days.

TRPL mapping: The correlated single photon detector provides a temporal resolution of up to 220 ps (PMA Series) in range of 185-800 nm, the image resolution is 0.625 μm for $CsPbBr_3$ films and 0.4 μm for CsFAMAPb$(IBr)_3$ (Figures 7 a, b). The power detector operation range is 0.5 nW - 500 mW. TRPL curve: The resolution has been used as 0.008 ns and the maximum resolution of synchronization channel of PicoHarp 300 is 4 ps resolution. Here curves fit error should be less than 5%. Angle - resolved PL: The positioner for the rotation of the collecting channel is assembled on the basis of a stepper motor, gearbox and encoder. The minimum step of such an assembly is $1^\circ/500 = 0.002^\circ$. Thus, the total incoming error at 360° rotation is no more than 0.5°. Due to all these factors, it was decided to measure the photoluminescence spectra in 1° increments.

It is important to note that various factors may contribute to experimental errors, includ-

ing but not limited to instabilities of laser equipment parameters, measurement inaccuracies, and material inconsistencies. However, through rigorous statistical analysis and the repetition of experiments under controlled conditions, here it has been minimized the influence of these potential sources of error.

References

(1) Solomonov, A. I.; Kushchenko, O. M.; Kasyanova, K. I.; Isaeva, S. B.; Shishkin, I. I.; Terekhov, D. Y.; Lazarenko, P. I.; Rybin, M. V.; Baturin, S. S.; Sinelnik, A. D. Switching topological charge of optical vortex by two-dimensional structures. *Applied Materials Today* **2024**, *37*, 102135.